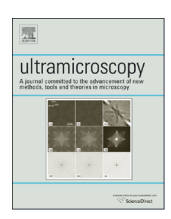
ELSEVIER

#### Contents lists available at ScienceDirect

### Ultramicroscopy

journal homepage: www.elsevier.com/locate/ultramic



# Experimental evaluation of the 'transport-of-intensity' equation for magnetic phase reconstruction in Lorentz transmission electron microscopy



Amit Kohn a,\*, Avihay Habibi b, Martin Mayo b

- <sup>a</sup> Department of Materials Science and Engineering, Faculty of Engineering, Tel Aviv University, 69978 Tel Aviv, Israel
- <sup>b</sup> Department of Materials Engineering, Ben-Gurion University of the Negev, 84105 Beer Sheva, Israel

#### ARTICLE INFO

Article history:
Received 15 April 2015
Received in revised form
20 September 2015
Accepted 26 September 2015
Available online 30 September 2015

Keywords: Lorentz transmission electron microscopy Transport of intensity equation Magnetic phase reconstruction

#### ABSTRACT

The 'transport-of-intensity' equation (TIE) is a general phase reconstruction methodology that can be applied to Lorentz transmission electron microscopy (TEM) through the use of Fresnel-contrast (defocused) images. We present an experimental study to test the application of the TIE for quantitative magnetic mapping in Lorentz TEM without aberration correction by examining sub-micrometer sized Ni<sub>80</sub>Fe<sub>20</sub> (Permalloy) elements. For a JEOL JEM 2100F adapted for Lorentz microscopy, we find that quantitative magnetic phase reconstructions are possible for defoci distances ranging between approximately 200 µm and 800 µm. The lower limit originates from competing sources of image intensity variations in Fresnel-contrast images, namely structural defects and diffraction contrast. The upper defocus limit is due to a numerical error in the estimation of the intensity derivative based on three images. For magnetic domains, we show quantitative reconstructions of the product of the magnetic induction vector and thickness in element sizes down to approximately 100 nm in lateral size and 5 nm thick resulting in a minimal detection of 5 T nm. Three types of magnetic structures are tested in terms of phase reconstruction: vortex cores, domain walls, and element edges. We quantify vortex core structures at a diameter of 12 nm while the structures of domain walls and element edges are characterized qualitatively. Finally, we show by image simulations that the conclusions of this experimental study are relevant to other Lorentz TEM in which spherical aberration and defocus are dominant aberrations.

© 2015 Elsevier B.V. All rights reserved.

#### 1. Introduction

Imaging the magnetic structure of materials at the nanometer scale is motivated by the scientific study of magnetic phenomena and the technological drive to develop new devices, in particular for information storage devices [1,2]. The magnetic structure can be imaged qualitatively and mapped quantitatively using transmission electron microscopy (TEM) in a variety of contrast modes, so-called 'Lorentz TEM' [3,4,52], for example, Fresnel-contrast defocused images. Magnetic imaging in the TEM is possible because in the presence of a magnetic (and electric) potential, the wave function of the electron undergoes a phase shift [5].

Consequently, quantitative mapping of the magnetic induction vector at nanometer scale spatial resolution can be extracted. However, measuring the phase of an electron wave exiting the sample is challenging because the phase component of the electron wave which reaches the imaging detector is lost due to the

E-mail address: akohn@post.tau.ac.il (A. Kohn).

quantum mechanical nature of the measurement. Additionally, the phase component is influenced by aberrations of the microscope and the signal collected at the detector further influenced by the modulation transfer function (MTF) of the charge-coupled device [6].

Here we examine experimentally quantitative magnetic imaging using the 'transport of intensity' equation (TIE) in conventional Lorentz TEM as a phase reconstruction methodology. By conventional Lorentz TEM, we refer to a microscope with a significant spherical aberration.

The principle of this methodology, developed by Teague for wave propagation in general [7], is based in the case of Lorentz TEM on Fresnel-contrast images. A focal series enables to correlate the intensity, phase and intensity derivative with respect to the direction of the wave propagation [8]. A detailed description on how this methodology was applied in this study is presented later.

The TIE approach for magnetic imaging in the Lorentz TEM can be a complementary methodology to off-axis electron holography. In terms of phase reconstruction, the TIE is more sensitive at higher spatial frequencies, while off-axis electron holography is better at lower spatial frequencies [9] leading to a suggestion to

<sup>\*</sup> Corresponding author.

combine both methodologies [10].

For practical application, the TIE methodology has several advantages compared to off-axis electron holography. First, it can be applied in most conventional TEMs, including those with reduced coherency of the electron source, e.g. LaB<sub>6</sub> [8,11]. The method is less demanding in terms of sample requirements. The sample is not required to be prepared so that the region of interest is placed near the vacuum, which may modify the micromagnetic structure. The field of view is larger than typically found in off-axis electron holography. Finally, the TIE approach is more convenient for in situ experiments.

The objective of this research is to test experimentally the quantitative capability of the TIE phase reconstruction approach specifically for magnetic imaging in conventional Lorentz TEM, as manifested in the measurement of the phase gradient, which relates to the product of the magnetic induction, B, and thickness of the sample, t. The aims of this examination are to determine the limit of detection, and the accuracy of the measured Bt product, as well as the spatial detection limit of magnetic structures.

Most reports on quantitative electron phase reconstructions using the TIE methodology are for electrostatic potentials in non-magnetic materials, e.g. Refs. [12–17]. The phase sensitivity of the TIE for the electrostatic potential phase step was estimated theoretically at  $\pi/20$  rad [18] and possible phase accuracy of up to  $\pi/300$  rad [9]

There are fewer reports on quantitative application of the TIE methodology to magnetic materials, typically applied to micrometer scale structures e.g. Refs. [11,19–22,53]. When applied to the study of magnetic materials, Masseboeuf et al. [23] studied a chemically ordered FePd thin film, reporting a *Bt* detection of several tens of *T* nm using an FEI Titan equipped with a dedicated Lorentz lens. A spatial resolution of 10 nm was estimated based on the detection of domain walls. Phatak et al. [24] applied the TIE to a three-dimensional reconstruction of the magnetic vector potential in a square 1 µm Permalloy element using a JEOL 2100F equipped with a Lorentz objective lens. The vector potential was probed at a spatial resolution of approximately 13 nm.

We tested experimentally the quantitative capability of the TIE by examining cases for phase reconstruction of lithographically patterned  $Ni_{80}Fe_{20}$  (Permalloy) elements in terms of varying lateral size and thicknesses. For quantitative analysis, the reconstructions were evaluated in terms of phase gradients along magnetic domains, which represent the Bt product. Additionally, the phase reconstruction from magnetic structures in the form of vortex cores,  $90^{\circ}$  domain walls, and elements edges were evaluated.

Experimentally, the limit of the magnetic detection for phase gradients in magnetic domains was found to be around 10 rad/ $\mu$ m, which in terms of the Bt product is 5 T nm in Permalloy elements sized laterally down to approximately 100 nm. The accuracy of the magnetic phase gradient reconstruction was under 1 rad/ $\mu$ m. In order to achieve quantitative phase reconstructions, both lower and upper limits for defoci distances were observed of 200  $\mu$ m and 800  $\mu$ m, respectively. The smallest magnetic structures that could be quantitatively detected were vortex cores 12 nm in diameter. The magnetic structures of domain walls and element edges were characterized qualitatively by phase reconstructions.

#### 2. Methodology

2.1. Magnetic phase reconstruction using the transport of intensity equation

Magnetic samples imaged at the nanometer scale are described as phase objects according to the Aharonov and Bohm equation [6], which quantifies the influence of electrostatic and magnetic potentials. By assuming a constant contribution from the electrostatic potential to the phase shift,  $\phi$ , of a sample with uniform thickness, t, and a constant magnetic induction, B, throughout the thickness of the sample, the phase change along one direction in a magnetic domain can be represented by:

$$\phi(x) = \frac{et}{\hbar} \int_{x_0}^{x_0 + x} B_y dx = \frac{e}{\hbar} B_y tx \tag{1}$$

where x is the direction in the plane of the sample perpendicular to the optic axis;  $B_y$  is the magnetic induction of the sample perpendicular to both x and the optic axis;  $x_0$  coordinate represents the location of a domain wall.

Therefore, the in-plane component of the magnetic induction vector,  $B_{\perp}$ , is derived by applying a gradient to the reconstructed phase:

$$\nabla \varphi(x, y) = -\frac{e}{\hbar} (B \times \hat{n}_z) t = -\frac{e}{\hbar} B_{\perp} t \tag{2}$$

where  $\hat{n}_z$  is a vector unit along the z direction, namely the optic axis

As noted, the TIE approach is a general phase reconstruction methodology, which was first applied to visible light microscopy [26], followed by neutrons [27], X-ray microscopy [28], and finally, the topic of this research, for fast electrons.

The TIE shows that the phase can be determined by intensity variation measurements:

$$\nabla_{\!\perp} \cdot [I(r_{\!\perp}, z) \nabla_{\!\perp} \phi(r_{\!\perp}, z)] = -k \frac{\partial I(r_{\!\perp}, z)}{\partial z}$$
(3)

The TIE correlates between image intensity, I, phase shift,  $\phi$ , of the electron wave-function and the derivative of the image intensity along the direction of the wave propagation, z (optic axis), where  $r_{\perp}$  represents the radial coordinate perpendicular to the optic axis and k represents the wavenumber of the fast electrons. Information transfer is attenuated by the square of the spatial frequency, meaning that transmission of low spatial frequencies is suppressed [29,30].

Solving differential Eq. (3) and optimizing the phase reconstruction result can be achieved by several routes. Pagannin and Nugent suggest a Fourier-transfom based approach [31], which was used in this study through the 'QPt' algorithm [32], as represented by Eq. (4):

$$\varphi(r_{\perp}, z) = -k \nabla_{\perp}^{-2} \nabla_{\perp} \left( \frac{1}{I(r_{\perp}, z)} \nabla_{\perp} \nabla_{\perp}^{-2} \frac{\partial I(r_{\perp}, z)}{\partial z} \right)$$
(4)

where  $\nabla_{\perp}^{-2}$  is the inverse Laplacian operator, which in the Fourier space is [33]:

$$\nabla_{\perp}^{-2} f(x, y) = F T^{-1} \left[ \frac{F T[f(x, y)]}{|q_{\perp}|^2} \right]$$
 (5)

The symbols FT and  $FT^{-1}$  represent forward and inverse Fourier transforms, respectively, and  $q_{\perp}$  is the spatial frequency vector normal to the propagation direction.

For solving the TIE equation, the intensity derivative with respect to the optic axis, z is estimated [15]. In practice, we acquire two defocused (Fresnel-contrast) images,  $I(r_{\perp}, -\Delta z)$  and  $I(r_{\perp}, +\Delta z)$ , and a Gaussian image,  $I(r_{\perp}, 0)$ . Due to small magnetic deflection angles, in this work down to several µrad, large defoci distances are required, typically  $100-1000~\mu m$ , for achieving Fresnel-contrast images with sufficient contrast. Consequently, alignment between defocused images is critical because of the practical large image rotation and change in magnification observed at the microscope. Barty et al. [34] and McVitie et al. [30] show that a misalignment of a single pixel is sufficient to

deteriorate quantitative phase reconstruction. This can be understood since information in Fresnel-contrast images originates from transition regions, such as magnetic information from domain walls, and electrostatic information from edges of the element. In order to achieve reproducible image alignment at sub-pixel accuracy for a large number of experiments, three Fresnel-contrast images were aligned with the 'Align 3\_TP' plugin for ImageJ [35].

#### 2.2. Micromagnetic simulations

Micromagnetic simulations of the equilibrium magnetic structure were used to evaluate the quantitative capability of the TIE approach for phase reconstruction. Simulations were performed by the 'Object Oriented Micromagnetic Framework' (OOMMF) package [36] and the 'LLG' software [37]. The cell size used was under 5 nm, which is less than the ferromagnetic exchange-interaction length for Permalloy [38]. Magnetic parameters for Permalloy are exchange stiffness,  $A=13\cdot 10^{-12}$  J/m, negligible anisotropy constant,  $K_u=100$  J/m³, and saturation magnetization,  $M_s=860\cdot 10^3$  A/m [39]. Micromagnetic simulations also determined a minimal distance between elements in order to prevent dipolar interactions as we compared experimental results to individual magnetic elements. The equilibrium micromagnetic structure was converted to magnetic phase variations of the electron wave based on Ref. [40]

#### 2.3. Fabrication and characterization of magnetic elements

Magnetic elements were fabricated on  $100 \times 100 \ \mu m^2$  windows of  $Si_3N_4$  membranes, 15 nm thick, supported on  $500 \ \mu m$  thick single crystal silicon wafers. Patterning was done by electron beam lithography on samples coated with a positive resist of polymethyl methacrylate. Permalloy films were then deposited using e-gun physical vapor deposition.

The deposition thicknesses of Permalloy layers were calibrated by cross sectional TEM analysis and atomic force microscopy (AFM), which also determined that the layers are smooth, with a standard deviation of 0.1 nm. The important definition of film thickness for this study is according to the effective magnetic thickness. Vibrating sample magnetometry measurements were based on saturation magnetization of the layer. Table 1 compares various thickness measurements showing that magnetic thicknesses are less than those determined in the TEM and AFM by up to 2 nm. This difference is attributed to a lower saturation moment in thin films or so-called 'dead layers', which refers to changes in the magnetic properties at the grain boundaries, interfaces and surfaces of the polycrystalline film [41]. Following these measurements, we calibrated sample thickness deposition according to the magnetic thickness.

Energy dispersive spectroscopy indicated that Fe content varied between 20% and 27 at% as compared to the 20 at% of the source material. The variations in composition are mostly associated with the quantitative accuracy of this spectroscopy methodology. Highangle annular dark-field scanning transmission electron microscopy Z-contrast analysis indicates that the composition across the layer is uniform. TEM analysis (phase-contrast, selected area

**Table 1** Examples of layer thickness measurements for calibration of deposition thickness (nm, errors are standard deviations).

VSM	TEM (cross section)	AFM	
$5.5 \pm 0.2$ $11.7 \pm 0.4$ $18.7 \pm 0.6$ $24.0 \pm 0.8$	$6 \pm 1$ $13.8 \pm 1.0$ $20.5 \pm 1.0$ $25 \pm 1$	$6.3 \pm 0.3$ $13.4 \pm 1.0$ $20 \pm 1$ $25.0 \pm 1.2$	

electron diffraction) determined that the crystal structure is FCC with a lattice parameter of  $0.35 \pm 0.01$  nm. The microstructure is polycrystalline, without preferred crystallographic orientation, with a grain size in the range of 5–7 nm.

Magnetic anisotropy was measured on Permalloy films deposited on an oxidized silicon wafer. Samples sized  $0.5 \times 0.5 \, \mathrm{cm}^2$  were used to measure the dependence of magnetic moment and coercive fields as a function of the direction of in-plane applied magnetic field. The area inside the hysteresis loop at each angle was measured and divided by the sample volume. These measurements were fitted to uniaxial anisotropy energy resulting in a constant of  $K_1 = 624 \pm 75 \, \mathrm{J/m^3}$ , which is negligible in determining the micromagnetic structure. Simulations undertaken with the above anisotropy value and using  $K_1 = 0 \, \mathrm{J/m^3}$  result in identical equilibrium micromagnetic structures.

#### 2.4. Lorentz TEM

All measurements, including structural analysis, were performed using a JEOL JEM 2100F transmission electron microscopy, equipped with a Schottky field emission gun and a biprism. This microscope was adapted and calibrated for Lorentz TEM as described in Ref. [25]. The optical configuration enabled a maximum nominal magnification of  $\times$  40 K. The objective lens was demagnetized and then an opposing current was used to reduce the residual field to under 1 Gauss as verified by a Hall probe holder. The spherical aberration coefficient is  $C_s{=}4.61\pm0.17$  m, and the chromatic aberration was calculated to be 87 mm. Therefore, the point resolution is approximately 2 nm. The minimal defocus step is  $3.02\pm0.01~\mu m$ ; for finer control of the defocus distance in order to achieve Gaussian conditions, a defocus step of 0.3  $\mu m$  is possible by mechanically translating the stage along the optic axis. The convergence semi-angle was estimated at 0.1 mrad.

For comparison of TIE phase reconstructions, off-axis electron holography measurements were undertaken using a biprism filament (0.6  $\mu$ m in diameter). The expected phase sensitivity and spatial resolution for off-axis electron holography are approximately  $\pi/25$  rad and 10 nm, respectively. The phase was reconstructed from the holograms using scripts of Arizona State University (e.g., Ref. [44]) within the Gatan Digital Micrograph software.

#### 2.5. Image simulations

For simulating Fresnel-contrast images in the transmission electron microscope, we used the algorithm developed by McVitie et al. [45]. To this algorithm we added the following components: optical parameters of the adapted JEOL JEM 2100F Lorentz TEM, modulation transfer function and shot noise of the Gatan Ultrascan charge-coupled device (CCD) detector, electrostatic potential of the sample (mean inner potential of Permalloy is 27.8 V [11]) and its specific geometry, especially at the edges, determined by the lithographic process. Due to limitation in sample fabrication and lithography processes, the element's edge is a step that was approximated as a Gaussian function spread across 10 to 20 nm from a fit to bright-field TEM images. This smeared edge structure is important to enable the Fourier-transform based algorithm to work. In case of an abrupt edge, namely the element's edge spans a single pixel, the Fourier transform based method applied here to solve the TIE fails due to high frequency information. We note that the edge profile of the element was not taken into account in the micromagnetic simulations calculated by the OOMMF algorithm.

The amplitude of the electron wave-function was estimated

<sup>&</sup>lt;sup>1</sup> Based on Refs. [6,42] and fringe spacing from Refs. [43,25].

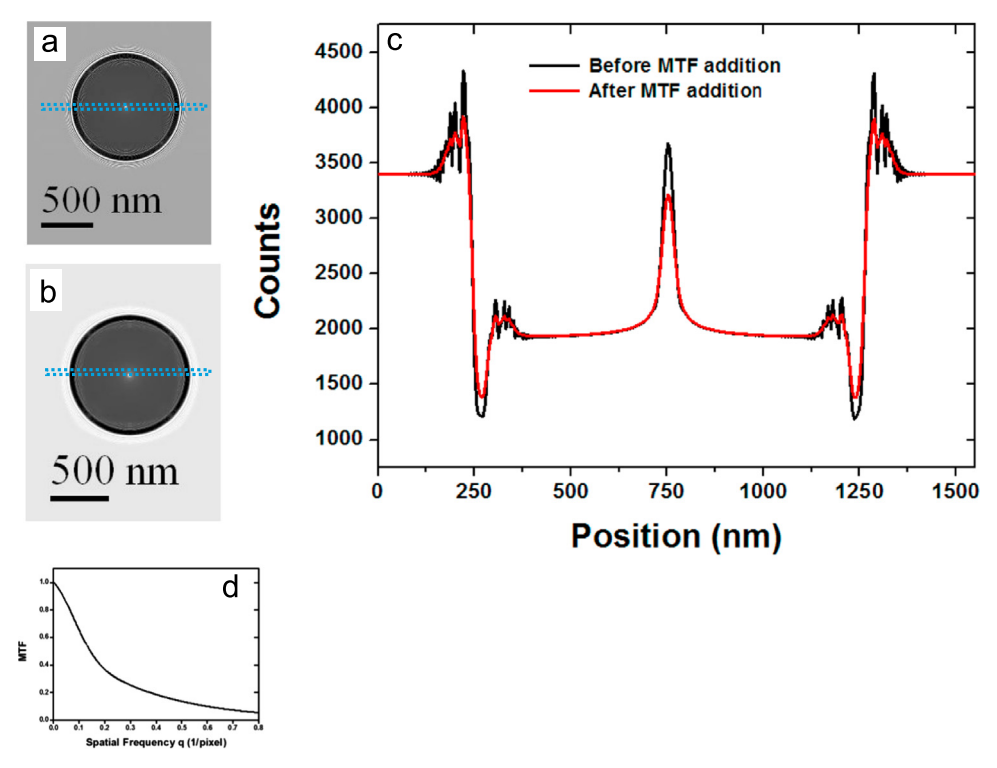
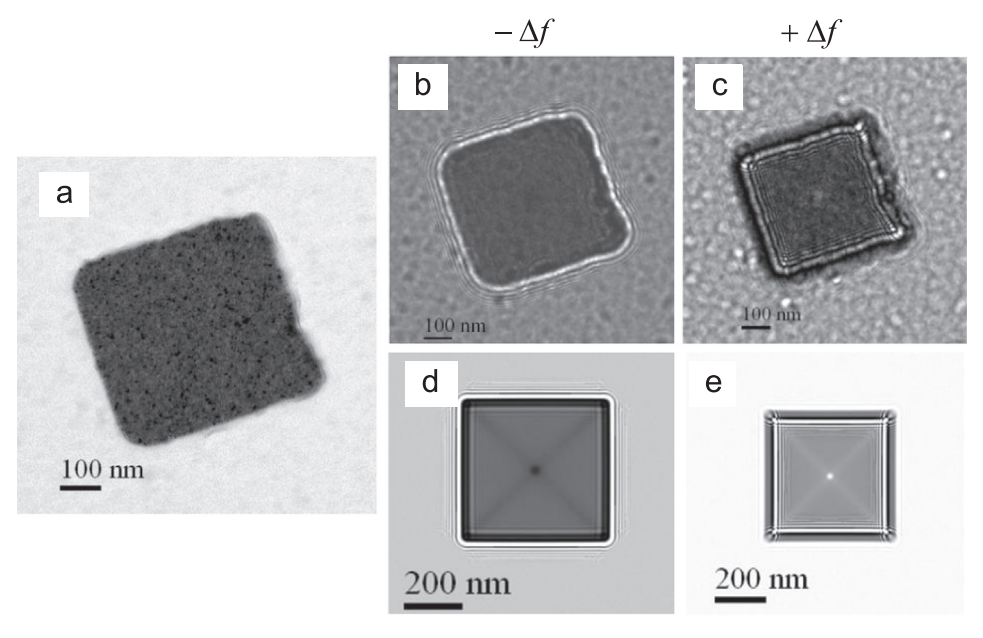


Fig. 1. Fresnel- contrast images of circular, 1  $\mu$ m in diameter, Permalloy element, 30 nm thick before (a) and after (b) MTF addition and their line profile (c) along the direction denoted schematically by the blue dashed line, (d) Modulation transfer function of the Gatan Ultrascan1000 CCD. (For interpretation of the references to color in this figure legend, the reader is referred to the web version of this article.)

experimentally from bright field images at Gaussian conditions. For the spatial frequencies examined in this work the CTF for the amplitude is approximately constant and close to a value of 1. Therefore, we approximate the Gaussian intensity as the square of the amplitude. Changes in magnification and rotation of the image due to the large defoci distances were not included in these simulations.

The MTF was measured according to the knife-edge method using the beam stopper of the microscope [46]. Fig. 1(d) shows the measured MTF of the Ultrascan CCD at a nominal magnification of

 $\times$  40 K, and  $\times$  2 binning conditions (1 k pixels  $\times$  1 k pixels image). The output images were calculated as a product of the simulated images with the relative attenuation of the MTF at corresponding frequencies. Fig. 1 demonstrates the contribution of the MTF to the Fresnel- contrast images, in this case of a *Permalloy* circular element, 1  $\mu m$  in diameter and 30 nm thick. Fresnel contrast intensities associated with the magnetic vortex (center) and the element's edge decrease after adding the contribution of the MTF.



**Fig. 2.** (a) Bright-field TEM image of a 30 nm thick, 0.5 μm square Permalloy element patterned on a Si<sub>3</sub>N<sub>4</sub> membrane. (b, c) experimental Fresnel-contrast images, underfocus and over-focus distances of  $\Delta f$ = 399 μm, respectively compared to equivalent simulated results (d, e). Note: (a–c) data from Ref. [25].

## 3. Evaluating the TIE methodology for magnetic phase reconstruction

We undertook comparisons of the TIE phase reconstruction methodology between experimental measurements and simulations to address the following points:

- 1. Accuracy of measuring the product of magnetic induction, *B*, and sample thickness, *t*.
- 2. Minimal Bt product value that is detected.
- Laterial spatial resolution: Minimal magnetic structure that is detected.

We demonstrate our approach to address the above points with an example, shown in Fig. 2, which is representative of dozens of elements examined in this research. The comparison is between experimental Fresnel-contrast images to simulated images based on micromagnetic simulations, in this case of a square Permalloy element, with a side length of 0.5  $\mu$ m, and 30 nm thick. Fig. 2(a) is a bright-field image (Gaussian defocus) of this element, obtained in the Lorentz mode, which highlights the polycrystalline structure. Fig. 2(b) and (c) are experimental Fresnel-contrast images, at under- and over-focus distances of 399 µm. Qualitatively, three sources of magnetic contrast are observed: bright and dark bands and the spot at the center of the element originate from domain walls and a vortex core structure, respectively, due to a magnetic flux-closure structure. The third source are Fresnel fringes observed at the edges of the elements, which originate both from changes in magnetic induction and the electrostatic mean inner potential. Fig. 2(d) and (e) are comparable Fresnel-contrast images simulated using the same optical conditions.

The reconstructed phase, in the form of equi-phase contour maps, from these simulated and experimental defocused image are shown in Fig. 3(a) and (b), respectively. In this presentation, the direction of the induction vector, *B*, is along the equi-phase line, and the magnitude of the vector is determined by the proximity of the contour lines (or gradient) perpendicular to the vector direction. Fig. 3(c) is the reconstructed phase of the same Permalloy square element measured by off-axis electron holography. Note that this off-axis electron holography result demonstrates two relative drawbacks when compared to Fresnel-contrast imaging and the TIE methodology: a smaller field of view, and lack of a reference hologram from the vacuum for this sample configuration, which degrades the quality of the reconstruction (see following).

A comparison of the phase values along the direction denoted schematically by the dashed red line in Fig. 3(b) is shown in Fig. 4 for the TIE reconstruction of Fresnel-contrast images at different defoci distances as well as compared to off-axis electron holography measurements. Qualitatively, the reconstructed phase

shows the electrostatic step at the edge of lithographically patterned elements due to the change in the mean inner potential, and the linear phase variations due to the magnetic domains. Within the transition region between the two magnetic domains, information about the core vortex may be expected.

For quantitative comparison, reconstructions were evaluated in terms of phase gradients within the magnetic domains in order to calculate the *Bt* product, in this case at an expected value of approximately 30 T nm. Phase gradients with respect to spatial position are shown in Fig. 4(b).

From this type of comparisons, we find that quantitative reconstructions are possible in a defoci window ranging approximately from 200  $\mu m$  to 800  $\mu m$ . For our experiments, these defoci distances adhere to the small defocus limit criterion, as presented by Beleggia et al. [18] and McVitie et al. [45], though Ishizuka et al. note that as the TIE is a form of the Schrödinger equation, a small defocus is not a prerequisite [29]. The reasons for incorrect magnetic phase reconstructions at defoci values under 200  $\mu m$  and above 800  $\mu m$  are discussed later.

Table 2 shows typical errors in determining the Bt product at different defoci distances. These values were estimated from all quantitative reconstructions, which were obtained at the same defocus distance. For our off-axis holography measurements, the Bt accuracy is 0.8 T nm. The reason for achieving better accuracy using the TIE methodology for defoci distances under 300  $\mu$ m may be due to the lack of a reference hologram and instabilities associated with the laboratory environment [25].

Fig. 5 shows examples of magnetic phase reconstructions for a range of elements in terms of size and geometry. From these types of comparisons, we conclude that correct magnetic phase reconstructions for Permalloy elements are possible down to approximately 100 nm in lateral size and 5 nm thick, which represents a minimum Bt detection of approximately 5 T nm, due to a phase gradient of 10 rad/ $\mu$ m, at an accuracy of 1 T nm.

The failure of quantitative TIE phase reconstructions at large defoci distances, approximately  $800~\mu m$ , is attributed to an error in the estimate of the image intensity derivative along the opticaxis, an explanation proposed by Allman and Ishizuka [29]. Here, the intensity derivative is estimated using two defocused images and an image at Gaussian defocus. Since only two defocused images are used, and representing the image derivative as a Taylor series, an error is introduced according to Eq. (6):

$$\frac{I(+\Delta z) - I(-\Delta z)}{2(\Delta z)} = \frac{\partial I}{\partial z} + O((\Delta z)^2)$$
 (6)

where I represents the image intensity,  $\Delta z$  is the defocus distance with respect to the Gaussian defocus, and z represents the spatial coordinates along the optic axis.

The use of two defocused images means that as the defocus distance is increased, the error in the approximation of the

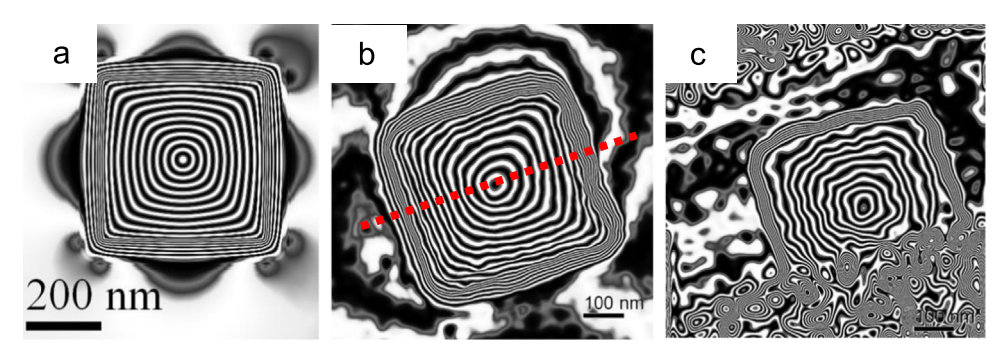


**Fig. 3.** Phase reconstructions (equi-phase presentation spaced at 1 rad) for a Permalloy square element, 30 nm thick, using the TIE approach applied to (a) Fresnel-contrast image simulations, (b) experimental Fresnel-contrast images (399 µm defocus). Results compared to phase reconstruction by (c) off-axis electron holography. Note: (b, c) data from Ref. [25]. (For interpretation of the references to color in this figure, the reader is referred to the web version of this article.)

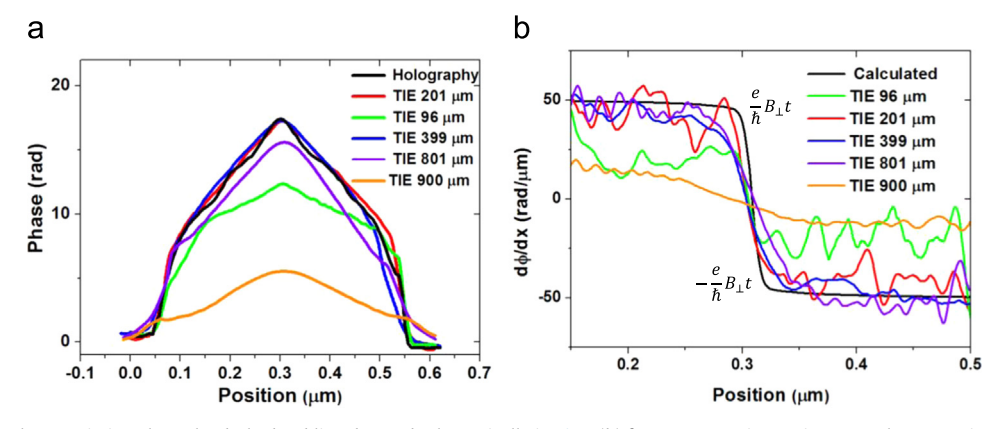


**Fig. 4.** (a) Values of the phase variation along the dashed red line denoted schematically in Fig. 3(b) for reconstructions using Fresnel-contrast images at defoci distances of  $96 \mu m$ ,  $201 \mu m$ ,  $399 \mu m$ ,  $801 \mu m$  and  $900 \mu m$ , and a comparison to phase reconstruction using off-axis electron holography. (b) First derivative of the reconstructed phase with respect to spatial position, which enables to determine the Bt product within the magnetic domain in comparison to the calculated value based on magnetometry and micromagnetic simulations. (For interpretation of the references to color in this figure legend, the reader is referred to the web version of this article.)

 Table 2

 Accuracy of measured Bt product at different defoci distances.

Defocus distance (μm)	Error in determining Bt (T nm)
200	0.5
300	0.6
400	0.8
600	1
800	1.6

intensity derivative is also increased according to the Taylor series. To demonstrate this explanation, we compare between experimental and simulated Fresnel contrast images at large defoci distances for a magnetic vortex core. Fig. 6 are experimental and simulated Fresnel-contrast images comparing image intensities across the vortex core in a circular Permalloy element, 1 µm in

diameter, 10 nm thick, at a defocus distance of  $900 \, \mu m$ . A significant increase or decrease in image intensity is observed at the vortex core. The background signal showing rapid intensity variations is due to the sources of noise, which are discussed later. The phase reconstruction using the TIE methodology failed in this case, as reported earlier. However, Fig. 6(e-g) shows agreement between simulated and experimental Fresnel-contrast images in terms of the intensity differences at the core.

Similar comparisons of the vortex core was undertaken for a square  $0.5 \,\mu m$  element,  $20 \,nm$  thick, for a wide range of defoci distances showing good agreement between simulated and experimental Fresnel-contrast images, as shown in Fig. 7.

Allman and Ishizuka [29] further estimate an error criterion for the allowed defocus with respect to the required spatial frequencies:

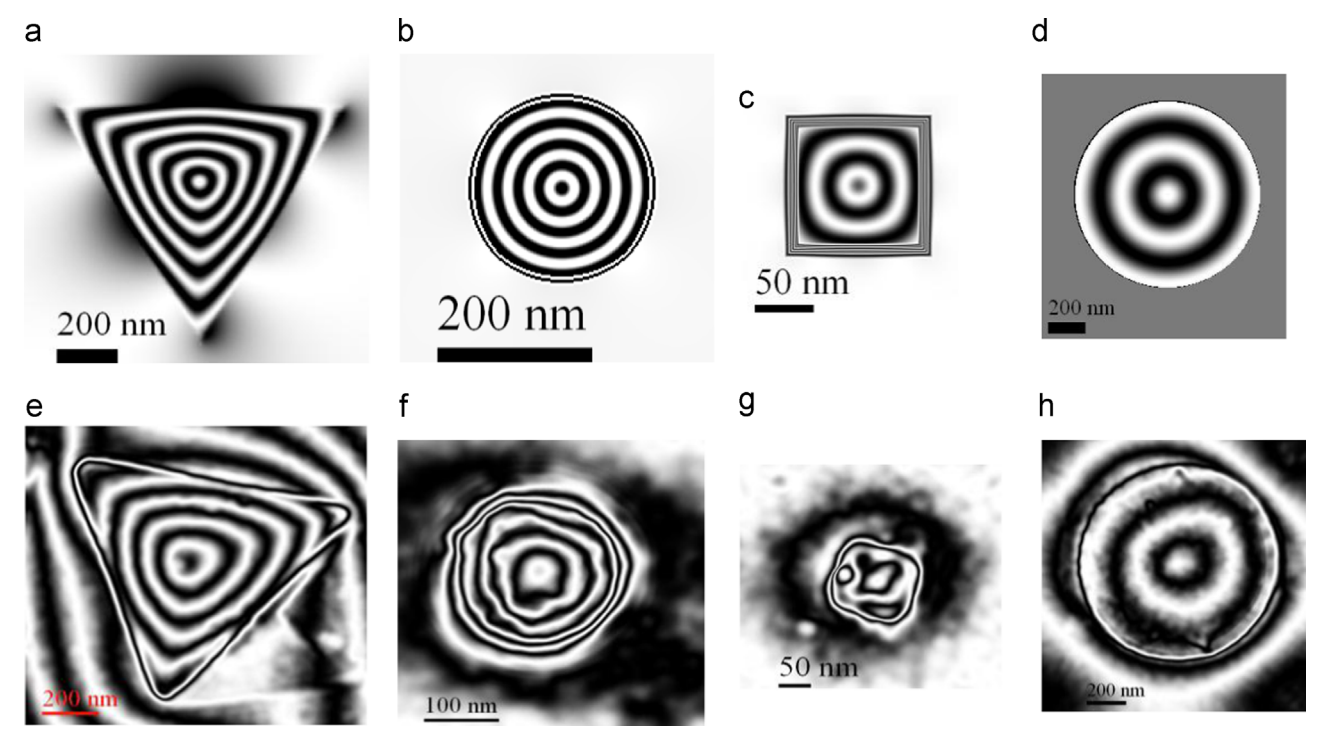


Fig. 5. Calculated (a–d) and experimental (e–h) eqi-phase contour maps (spaced at 1 rad) for triangular element, 1  $\mu$ m diagonal, 10 nm thick (a, e), circular element, 250 nm in diameter, 20 nm thick (b, f), square element, 130 nm edge length, 10 nm thick (c, g) and circular element, 1  $\mu$ m in diameter, 5 nm thick (d, h). The phase reconstruction of the triangle (e), square (g) and circular (h) elements were obtained from Fresnel-contrast images at a defocus distance of 600  $\mu$ m while the phase reconstruction of the circular element (f) was obtained from Fresnel-contrast images at a defocus distance of 198  $\mu$ m.

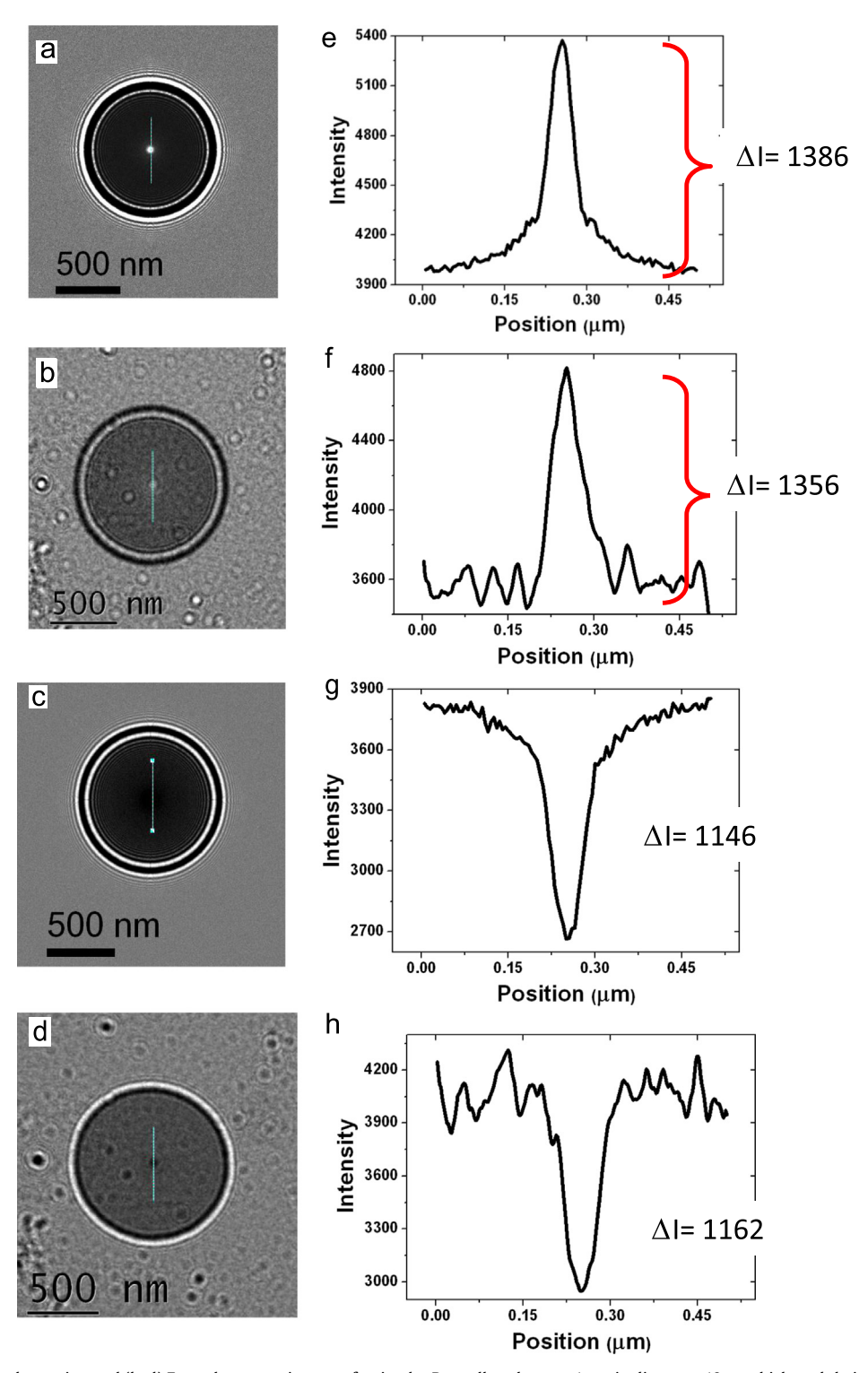


Fig. 6. Simulated (a, c) and experimental (b, d) Fresnel-contrast images of a circular Permalloy element, 1  $\mu$ m in diameter, 10 nm thick, and their intensity profile (e-h) along the green dashed line at a defocus distance of 900  $\mu$ m. Figures a, b are the over-focused images and c, d are the under-focused images.

$$\pi\lambda(2\Delta z)g_{max}^2 \le \sqrt{6} \tag{7}$$

where  $g_{max}$  is the highest spatial frequency included in the image. Therefore, for a defocus distance,  $\Delta z$ , of 800  $\mu$ m, significant phase information varying at distances smaller than approximately 70 nm will not be reconstructed. This value is in agreement with our experimental observations because, as demonstrated later, this is the approximate scale for magnetic and electrostatic

phase variations in the samples examined here.

We note that Martin et al. [47] determined an upper defocus limit for TIE phase reconstructions also due to spatial incoherence. Using their criterion for  $g_{max}$  determined when the Gaussian wave function drops to 95% of its maximum yields:

$$\pi\alpha(\Delta z)g_{\text{max}} \le 0.05 \tag{8}$$

Where  $\alpha$  is the convergence semi-angle of the source leading to

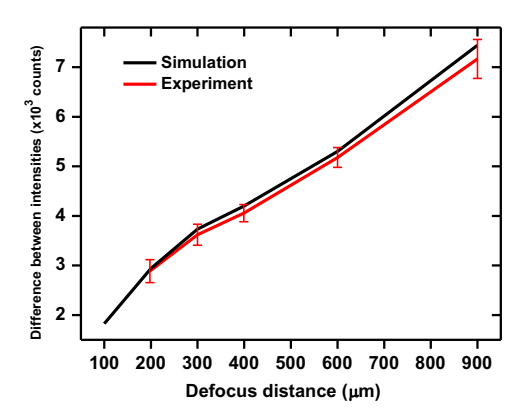


**Fig. 7.** Comparison of image intensity differences at the vortex core of a square Permalloy element,  $0.5 \,\mu m$ ,  $20 \,nm$  thick between simulated and experimental Fresnel-contrast images, for a range of defoci distances. (For interpretation of the references to color in this figure, the reader is referred to the web version of this article.)

spatial incoherence. In this case, for a defocus distance,  $\Delta z$ , of 800  $\mu m$ , and a convergence semi-angle of 0.1 mrad, significant phase information varying at distances smaller than approximately 5  $\mu m$  will not be reconstructed. Therefore, this criterion appears, when compared to our experimental data, to be too strict, for quantitative reconstruction of the magnetic phase.

The upper limit for defoci distances for quantitative phase reconstructions implies that we should reduce the defocus distance as much as possible, which is expected to improve spatial resolution for phase reconstruction [45,50,51] and also simplify image alignment. However, as the defocus distance is reduced, the intensity of magnetic signals such as domain walls, are reduced until they are comparable to other sources of intensity variations. For the samples tested here, these competing sources are: diffraction contrast of the polycrystalline Permalloy element, thickness variations in the sample, defects in the amorphous SiN membrane, photoresist leftover contamination on the elements, and CCD shot-noise. The influence of these sources of noise in the Fresnel-contrast images can be observed in Fig. 5(e-h), which is the reconstructed phase using the TIE methodology. Compare these results to the reconstructed phase from simulated Fresnelcontrast images Fig. 5(a-d). In these results, a constant and uniform phase is observed in the regions around the element, whereas the experimental results shows phase variations. The contribution of noise originating from CCD shot-noise as well as artifacts in the reconstruction algorithm was estimated by images recorded in a vacuum region. Applying the TIE algorithm for images recorded at defocus distances of 99µm results in phase variations up to 0.4 rad.

The polycrystalline structure of Permalloy introduces diffraction contrast, which in the context of magnetic phase reconstruction, is an additional source of noise as seen in Fig. 8(a). Dark regions in this image are grains that fulfill Bragg conditions. The effect of this contrast exists even when the defocus distance is increased and can occasionally cause the magnetic signal to be undetectable. As an example, Fig. 8(d) shows that at low defoci distances, the magnetic vortex core signal cannot be distinguished from this noise, as well as defects in the SiN substrate.

Beleggia et al. [18] proposes a Michelson visibility (( $I_{max}-I_{min}$ )) of 3% as a lower limit for defocus. Our observations, at

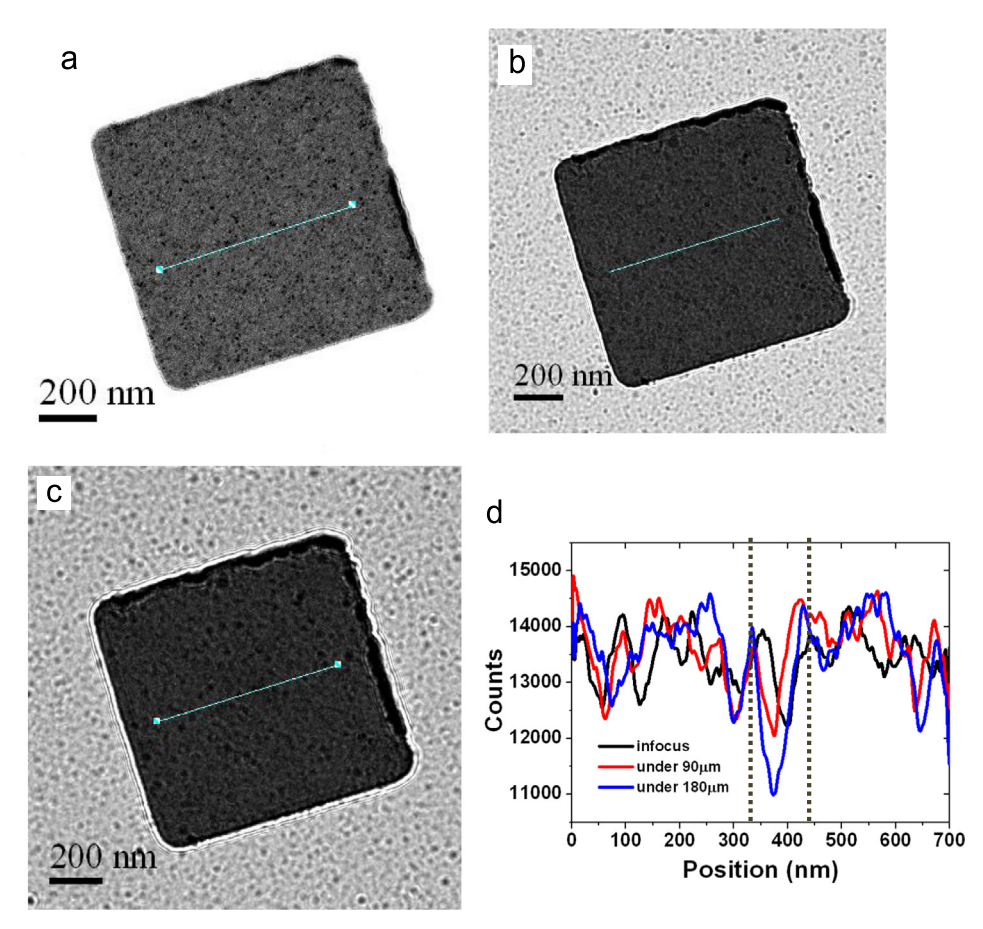
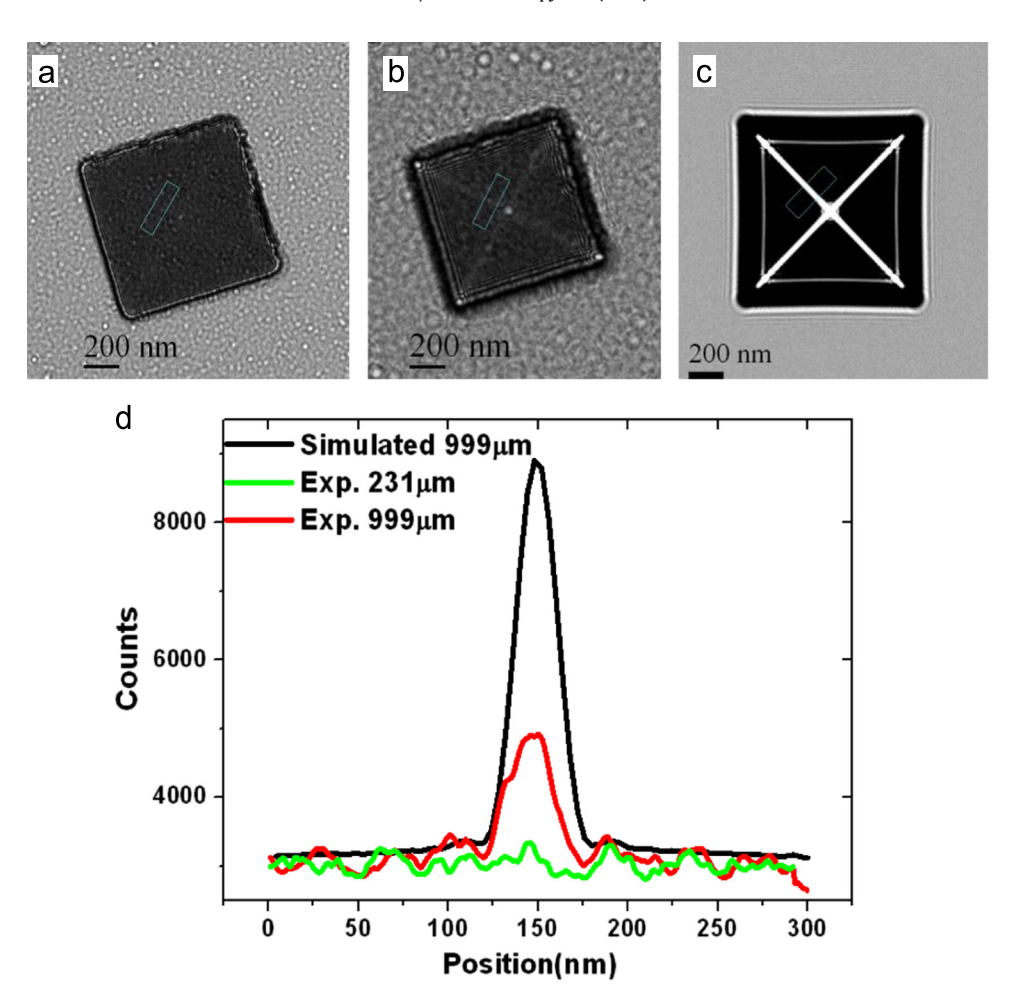


Fig. 8. (a) Bright-field (Gaussian defocus) image for a square 1  $\mu$ m element, 30 nm thick and Fresnel contrast images at defocus distances (under) of 90  $\mu$ m (b) and 180  $\mu$ m (c) Intensity line profiles for the above images along directions denoted schematically by the green lines (d). (For interpretation of the references to color in this figure legend, the reader is referred to the web version of this article.)



**Fig. 9.** Fresnel-contrast images of a square Permalloy 1  $\mu$ m element, 40 nm thick, at a defocus distance of 231  $\mu$ m (a), 999  $\mu$ m (b) (experimental) and a simulated Fresnel-contrast image (c) at defocus distance of 999  $\mu$ m. Intensity profiles of all images (d) along the direction denoted schematically by green dashed line. (For interpretation of the references to color in this figure legend, the reader is referred to the web version of this article.)

 $200 \,\mu m$  defocus, for example see Fig. 8d, are of a visibility of 7–10%. This increase in the visibility limit is attributed to the specific competing contrast sources described previously.

This last figure (and also the example shown in Fig. 9, see following) demonstrates that we do not observe a strong correlation between the noise contributions and the defocus distance. However, at a defocus distance of around 200  $\mu m$ , the noise contribution is comparable to the magnetic signal, meaning that we cannot achieve quantitative phase reconstructions at smaller defoci distances.

## 3.1. Sources of magnetic signal for testing the magnetic sensitivity of the TIE methodology

The magnetic signal in patterned elements originates from several sources. For example, in the case of patterned square elements showing flux closure, the magnetic phase variation originates from three sources: vortex core, 90° domain walls, and edges (Fresnel fringes).

In order to evaluate whether TIE phase reconstruction enables to characterize quantitatively the magnetic structures, the three sources were evaluated in terms of Fresnel-contrast images and the TIE phase reconstruction.

Domain walls: At low defoci distances, under 300  $\mu m$ , it is difficult to distinguish between signal and background noise as demonstrated in Fig. 9(a) for a square Permalloy 1  $\mu m$  element, 40 nm thick at a defocus distance of 231  $\mu m$ . At larger defoci distances, the domain wall signal is distinguished, Fig. 9(b). However,

when compared to the equivalent simulated Fresnel images, the measured intensity variations are smaller than in the simulated image. Additionally, at large defoci distances, e.g. the over-focus conditions seen in Fig. 9(b), Fresnel fringes from the edge of the element can overlap with intensity variations due to the domain wall and therefore degrade this signal.

We tested whether the reconstruction of the domain wall is quantitative by measuring the width of the domain wall. For example, a comparison between TIE reconstructed phase from simulated and experimental Fresnel-contrast images is presented for a square Permalloy 0.5  $\mu m$  element, 20 nm thick in terms of the width of the domain wall. For quantitative comparisons, we applied a functional definition that the width of the domain wall spans from maximum to minimum of the third derivative of the reconstructed phase with respect to spatial position. Applying this method to the calculated phase, which is derived from micromagnetic simulations for the element described above, the width of the 90° domain wall is 28 nm.

The comparison of the width of the 90° domain wall was undertaken for a wide range of defoci distances demonstrating a lack of quantitative agreement between simulated and experimental values as shown in Table 3.

The TIE shows a quantitative failure in determining the width and therefore the magnitude of the magnetic signal at these domain walls. However, the TIE does display qualitatively the presence of the domain wall region in the correct location in the reconstructed phase. This statement is demonstrated by comparing square, triangular and circular elements (e.g. Figs. 3, 5, and 6). The

**Table 3**Comparison between simulated and experimental measurements of domain wall widths measured from the reconstructed electron phase using the TIE methodology at different defoci distances.

Defocus distance (µm)	Simulated domain wall width (nm)	Experimental domain wall width (nm)	
50 100	30 32	Incorrect reconstructions	
201	43	$117 \pm 23$	
300 399	47 50	124 ± 17 125 + 31	
600	56	$131 \pm 27$	

square and triangular elements show, qualitatively, domain walls in the correct position compared to micromagnetic simulations, while the circular elements do not show domain wall, as expected for this micromagnetic vortex structure.

Edges of elements: the Lorentz force applied to fast electrons affects the location of Fresnel fringes resulting in a difference between magnetic and non-magnetic samples having the same thickness and mean inner potential, as shown in Fig. 10. A comparison was made between simulated and experimental results in terms of location of the periodic fringes and their intensity at various defoci distances. We observe agreement in the spatial location of the Fresnel fringes for all defoci distances as demonstrated in Fig. 10(d). Regarding intensity difference of these fringes, experimental images show lower intensity differences than in the case of simulated images. However, these comparisons are

**Table 4**Simulated and experimental measurements of the element edge and magnetic core for the element shown in Fig. 10 at various defoci distances using the TIE methodology.

Defocus dis- tance (μm)	Edge width (nm)		Core diameter (nm)	
	Simulated	Experimental	Simulated	Experimental
50	16	Incorrect	14	Incorrect
100	24	reconstruction	16	reconstruction
201	34	$37.2 \pm 7.8$	23	$27.5 \pm 2.6$
300	42	$43.0 \pm 5.6$	29	$33.1 \pm 4.3$
399	49	$49.7 \pm 4.6$	36	$35.8 \pm 5.7$
600	55	$57.5 \pm 5.7$	42	$44.1 \pm 14.4$
800	61	Incorrect reconstruction	49	Incorrect reconstruction

significantly better than in the case of domain walls. Qualitatively, it can be seen that at different locations of the element edge, variations in the intensities exist, which we attribute to leftover contamination from the photoresist on the elements.

Vortex core: a comparison between the reconstructed phase obtained from experiments and simulations was done for a variety of elements, examining the diameter of the core and comparing to an electrostatic signal step at the edge of the element. The diameter of the vortex core was functionally defined as spanning from maximum to minimum of the third derivative of the phase with respect to spatial position. The width of the element edge was defined using a similar approach, in this case the second

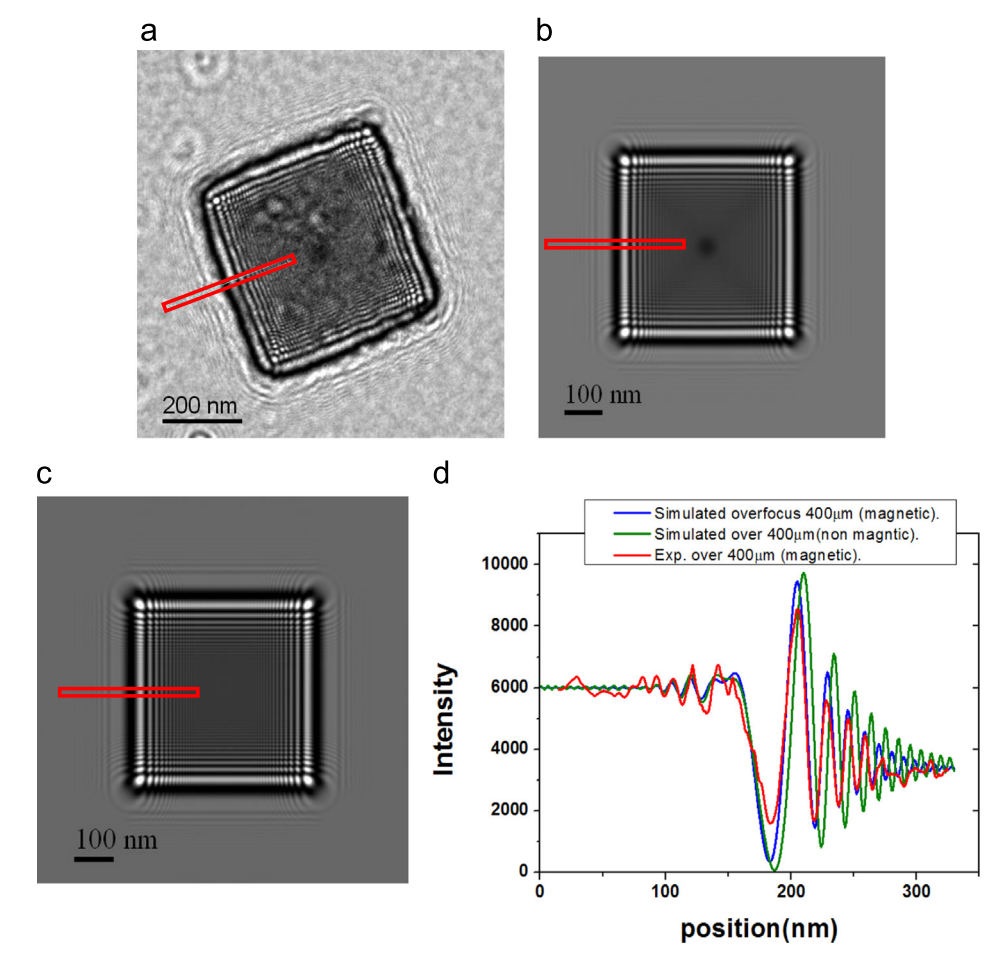


**Fig. 10.** (a) experimental Fresnel contrast image at a defocus (over) distance of  $400 \, \mu m$  for a square Permalloy  $0.5 \, \mu m$  element,  $20 \, nm$  thick and its equivalent simulated results with (b) and without (c) the magnetic contribution. Image (d) is a line profile along the direction denoted schematically by the red rectangle in a, b and c. (For interpretation of the references to color in this figure legend, the reader is referred to the web version of this article.)

**Table 5**Comparison of optical properties of microscopes used for Lorentz TEM.

	Adapted JEOL 2100F [25]	JEOL 2100F Lorentz [48]	Tecnai F20 Lorentz [6]	Titan (Cs-ad- justed) Lorentz [49]
E (keV) $C_s$ (mm) $C_c$ (mm) Point resolution (nm) (Scherzer defocus)	200 4600 87 1.96	200 108.7 16 0.77	200 8000 41 2.25	300 10 93 0.35

#### derivative.

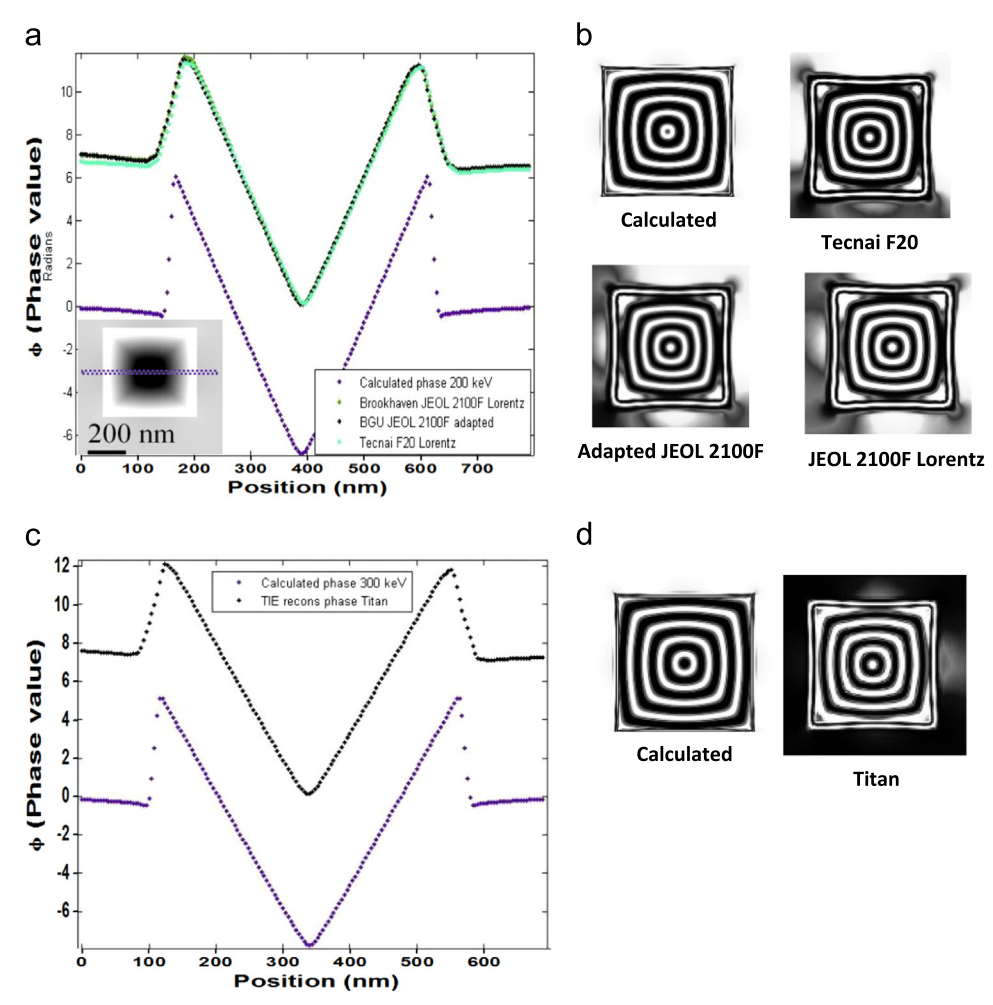
In experimental phase reconstructions, the diameter of the core was calculated for all angular directions through the core. For the width of the elements' edge, around 20 measurements were undertaken from each element so that we present the average value and the error is estimated as the standard deviation. Table 4 compares between simulated and experimental results for the magnetic core and the electrostatic step obtained for the element shown in Fig. 10. In this element, successful reconstructions were obtained at defoci distances of 201, 300, 399 and 600 µm.

Table 4 indicates agreement between simulations and experimental results. The micromagnetic simulation of this element shows that magnetic moments align into the plane of the element

approximately 6 nm from the center of the magnetic core so that the expected diameter of this region is 12 nm. The value measured from the calculated magnetic phase, according to our technical definition of a core diameter, is indeed approximately 10 nm. The measured increase in the diameter of the vortex core and width of the element edge as the defocus distance increases is attributed to the decrease in spatial resolution of the reconstructed phase. We note that this conclusion is dependent on the samples we tested. If we had tested the TIE methodology on materials with large magnetocrystalline anisotropy, the diameter of the magnetic vortex core is smaller. Therefore, it is possible that better spatial detection using the TIE methodology can be achieved.

#### 3.2. Applicability to Lorentz TEM

Finally, we consider whether the above experimental study is strongly microscope dependent. Therefore, we compare several conventional Lorentz TEMs by image simulations in order to examine whether our conclusions are relevant to other instruments. We note that our comparisons are to microscopes with non-negligible spherical aberration, as our image simulations are based on a contrast transfer function described by defocus and spherical aberration. Additionally, to these simulations, we do not add the MTF so as to focus on the role of optical configuration. Table 5 presents optical parameters of several microscopes operated in the Lorentz mode: an adapted JEOL JEM 2100F [25], a dedicated Lorentz JEOL JEM 2100F



**Fig. 11.** (a, c) Calculated phase values from the micromagnetic structure of a Permalloy 0.5  $\mu$ m square, 40 nm thick element (a-200 kV c-300 kV accelerating voltages) and simulated phase reconstructions using the TIE at a defocus distance of 200  $\mu$ m for microscopes detailed in Table 1 for (inset a: calculated phase; The violet rectangle shows schematically the line profile for the phase values). (b, d) Phase-contours presentation (spaced at intervals of  $\pi$  rad) for the presented results in a and c. (For interpretation of the references to color in this figure legend, the reader is referred to the web version of this article.)

[48], FEI Tecnai F20 [6], and an FEI Titan in which the aberration correction lenses were used to setup the Lorentz mode and reduce the spherical aberration down to 10 mm [49].

According to our image simulations, for example, Fig. 11, we do not observe a significant difference in the phase reconstruction capabilities of the TIE between Lorentz TEMs with varying values of the spherical aberration down to 10 mm. Fig. 11(b) and (d) shows the calculated magnetic phase from the micromagnetic structure of a Permalloy 0.5  $\mu$ m square sample, 40 nm thick. The phase values in the line scan are shown across two magnetic domains and the vortex core. This calculation is compared to the reconstructed phase using the TIE methodology with the optical parameters of the various Lorentz TEMs. Fig. 11(c) and (d) compares between the calculated phase and the TIE phase reconstruction for a Titan  $C_s$ -corrected Lorentz TEM. The phase results are presented in the form of equi-phase contour maps, spaced at  $\pi$  rad between lines.

Similar comparisons were done for additional Permalloy square samples down to a size of  $100 \times 100 \times 10~\text{nm}^3$ . Here too, no significant influence of the spherical aberration was observed. This result may be understood by the relative weak influence of the spherical aberration on the contrast transfer function at the relevant spatial frequencies examined here.

For microscopes where significant reduction of the spherical aberration (down to several  $\mu$ m) and a magnetic field free region for the sample are possible, several benefits are expected, for example reducing delocalization effects on field emission microscopes. Therefore, smaller defocus distances can be used and a higher signal-to-noise ratio, thus achieving spatial resolutions around 1 nm [50,51,53,54].

#### 4. Summary

We report the following experimental observations to the questions raised regarding quantitative evaluation of the TIE specifically for magnetic phase reconstruction in Lorentz TEM where spherical aberration and defocus are the dominant aberrations:

The limit of magnetic detection for the phase gradient was found to be approximately  $10 \text{ rad/}\mu\text{m}$ , which in terms of the Bt product is 5 T nm in Permalloy elements sized laterally down to around 100 nm. The accuracy of magnetic phase gradient reconstruction was under  $1 \text{ rad/}\mu\text{m}$ .

The smallest magnetic structures that could be quantitatively detected were vortex cores approximately 12 nm in diameter. It may be possible that smaller vortex cores can be detected, which requires testing on samples fabricated from materials with large magnetocrystalline anisotropy.

Magnetic phase variations at  $90^{\circ}$  domain walls and edges of elements are qualitatively reconstructed, with the latter closer to simulated values.

Quantitative reconstructions for the magnetic elements examined here were achieved at a defocus range between 200  $\mu m$  and 800  $\mu m$ . The lower limit is attributed to a visibility limit of magnetic contrast with competing sources. The upper limit is due to a numerical error in the estimation of the intensity derivative based on two Fresnel-contrast images around the Gaussian image.

#### Acknowledgments

We thank the Ilse Katz Institute for Nanoscale Science and Technology at Ben-Gurion University of the Negev for accessing the JEOL JEM 2100F TEM adapted for Lorentz TEM.

#### References

- A.K. Petford-Long, A. Kohn, T. Bromwich, V. Jackson, F. Castano, L.J. Singh, Application of TEM to the development of information storage materials, Thin Solid Films 505 (2006) 10–15.
- [2] M. Tanase, A.K. Petford-Long, In situ TEM observation of magnetic materials, Microsc. Res. Tech. 72 (2009) 187–196.
- [3] J.N. Chapman, The investigation of magnetic domain structures in thin foils by electron microscopy, J. Phys. D: Appl. Phys. 17 (1984) 623–647.
- [4] A.K. Petford-Long, J.N. Chapman, in: H. Hopster, H.P. Oepen (Eds.), Magnetic Microscopy of Nanostructures, Springer-Verlag, Berlin, 2004.
   [5] M.R. McCartney, D.L. Smith, Electron bolography: phase imaging with papers.
- [5] M.R. McCartney, D.J. Smith, Electron holography: phase imaging with nanometer resolution, Annu. Rev. Mater. Res. 37 (2007) 729–767.
- [6] H. Lichte, M. Lehmann, Electron holography—basics and applications, Rep. Prog. Phys. 71 (2008) 016102.
- [7] M.R. Teague, Deterministic phase retrieval: a Green's function solution, J. Opt. Soc. Am. 73 (1983) 1434–1441.
   [8] M. De Graef, Y. Zhu, Quantitative noninterferometric Lorentz microscopy, J.
- Appl. Phys. 89 (2001) 7177.
- [9] C.T. Koch, A. Lubk, Off-axis and inline electron holography: a quantitative comparison, Ultramicroscopy 110 (2010) 460–471.
- [10] C. Ozsoy-Keskinbora, C.B. Boothroyd, R.E. Dunin-Borkowski, P.A. van Aken, C. T. Koch, Hybridization approach to in-line and off-axis (electron) holography for superior resolution and phase sensitivity, Sci. Rep. 4 (2014) 7020.
- [11] A. Kohn, A.K. Petford-Long, T.C. Anthony, Magnetic potential in patterned materials determined using energy-dependent Lorentz phase microscopy, Phys. Rev. B 72 (2005) 014444.
- [12] P. Donnadieu, M. Verdier, G. Berthome, P. Mur, Imaging a dense nanodot assembly by phase retrieval from TEM images, Ultramicroscopy 100 (2004) 79–90
- [13] T.C. Petersen, V.J. Keast, K. Johnson, S. Duvall, TEM-based phase retrieval of p-n junction wafers using the transport of intensity equation, Phil. Mag. 87 (24) (2007) 3565–3578.
- [14] T.C. Petersen, V.J. Keast, D.M. Paganin, Quantitative TEM-based phase retrieval of MgO nano-cubes using the transport of intensity equation, Ultramicroscopy 108 (2008) 805–815.
- [15] M. Mitome, K. Ishizuka, Y. Bando, Quantitativeness of phase measurement by transport of intensity equation, J. Electron Microsc. 59 (1) (2010) 33–41.
- [16] T. Latychevskaia, P. Formanek, C.T. Koch, A. Lubk, Off-axis and inline electron holography: experimental comparison, Ultramicroscopy 110 (2010) 472–482.
- [17] C. Koch, Towards full-resolution inline electron holography, Micron 63 (2014) 69–75.
- [18] M. Beleggia, M.A. Schofield, V.V. Volkov, Y. Zhu, On the transport of intensity technique for phase retrieval, Ultramicroscopy 102 (2004) 37–49.
- [19] V.V. Volkov, Y. Zhu, Phase imaging and nanoscale currents in phase objects imaged with fast electrons, Phys. Rev. Lett. 91 (4) (2003) 043904.
- [20] V.V. Volkov, Y. Zhu, Lorentz phase microscopy of magnetic materials, Ultramicroscopy 98 (2004) 271–281.
- [21] A. Masseboeuf, O. Fruchart, F. Cheynis, N. Rougemaille, J.-C. Toussaint, A. Marty, P. Bayle-Guillemaud, Micromagnetic study of flux-closure states in Fe dots using quantitative Lorentz microscopy, Ultramicroscopy 115 (2012) 26–34
- [22] E. Humphrey, C. Phatak, A.K. Petford-Long, M. De Graef, Separation of electrostatic and magnetic phase shifts using a modified transport-of-intensity equation, Ultramicroscopy 139 (2014) 5–12.
- [23] A. Masseboeuf, C. Gatel, P.B. Guillemaud, A. Marty, J.C. Toussaint, Lorentz microscopy mapping for domain wall structure study in L1<sub>0</sub>FePd thin films, Ultramicroscopy 110 (2009) 20–25.
- [24] C. Phatak, A.K. Petford-Long, M. De Graef, Three-dimensional study of the vector potential of magnetic structures, Phys. Rev. Lett. 104 (2010) 253901.
- [25] A. Kohn, A. Habibi, Adapting a JEM-2100F for Magnetic Imaging by Lorentz TEM, JEOL News 47 (2012) 17–22.
- [26] A. Barty, K.A. Nugent, D. Paganin, A. Roberts, Quantitative optical phase microscopy, Opt. Lett. 23 (11) (1998) 817–819.
- [27] B.E. Allman, P.J. McMahon, K.A. Nugent, D. Paganin, D.L. Jacobson, M. Arif, S. A. Werner, Phase radiography with neutrons, Nature 408 (2000) 158–159.
- [28] S. Paganin, S.C. Mayo, T.E. Gureyev, P.R. Miller, S.W. Wilkins, Simultaneous phase and amplitude extraction from a single defocused image of a homogeneous object, J. Microsc. 206 (2002) 33–40.
- [29] K. Ishizuka, B. Allman, Phase measurement of atomic resolution image using transport of intensity equation, J. Electron Microsc. 54 (2005) 191–197.
- [30] S. McVitie, D.T. Ngo, Quantitative measurements of phase using the transport of intensity equation, J. Phys. 126 (2008) 012041.
- [31] D. Paganin, K.A. Nugent, Noninterferometric phase imaging with partially coherent light, Phys. Rev. Lett. 80 (1998) 2586.
- [32] A TIE plug-in for DigitalMicrograph (Gatan), see (http://www.hremresearch.com/Eng/plugin/QPtEng.html).
- [33] V.V. Volkov, Y. Zhu, M. De Graef, A new symmetrized solution for phase retrieval using the transport of intensity equation, Micron 33 (2002) 411–416.
- [34] A. Barty, D. Paganin, K. Nugent, Phase retrieval in lorentz microscopy, in: M. De Graef, Y. Zhu (Eds.), Magnetic Imaging and its Applications to Materials, Academic Press, San Diego, 2001.
- [35] Align3\_TP plugin for ImageJ, J. Anthony Parker, Beth Israel Deaconess Medical Center, Boston, MA.
- [36] M.J. Donahue, D.G. Porter, OOMMF User's Guide, Version 1.0. Interagency

- Report NISTIR 6376, National Institute of Standards and Technology, Gaithersburg, 1999.
- [37] Michael R. Scheinfein, (http://llgmicro.home.mindspring.com/index.htm).
- [38] G.S. Abo, Y.-K. Hong, B.C. Choi, M.J. Donahue, S. Bae, J. Jalli, J. Park, J. Lee, M. H. Park, S.H. Gee, Micromagnetic computer simulated scaling effect of S-shaped permalloy nano-element on operating fields for AND or OR Logic, IEEE Trans. Magn. 48 (2012) 5.
- [39] M. Barthelmess, C. Pels, A. Thieme, G. Meier, Stray fields of domains in permalloy microstructures—measurements and simulations, J. Appl. Phys. 95 (2004) 5641–5645.
- [40] M. Mansuripur, Computation of electron diffraction patterns in Lorentz electron microscopy of thin magnetic films, J. Appl. Phys. 69 (1991) 5890.
- [41] M. Vsiansk, M. Sob, Magnetically dead layers at sp-impurity-decorated grain boundaries and surfaces in nickel, Phys. Rev. B 84 (2011) 014418.
- [42] W.J. de Ruijter, J.K. Weiss, Detection limits in quantitative off-axis electron holography, Ultramicroscopy 50 (1993) 269–283.
- [43] Y.Y. Wang, J. Li, A. Domenicucci, J. Bruley, Variable magnification dual lens electron holography for semiconductor junction profiling and strain mapping, Ultramicroscopy 124 (2013) 117–129.
- [44] M.R. McCartney, N. Agarwal, S. Chung, D.A. Cullen, M.-G. Han, K. He, L. Li, H. Wang, L. Zhou, D.J. Smith, Quantitative phase imaging of nanoscale electrostatic and magnetic fields using off-axis electron holography, Ultramicroscopy 110 (2010) 375–382.
- [45] S. McVitie, M. Cushley, Quantitative Fresnel Lorentz microscopy and the transport of intensity equation, Ultramicroscopy 106 (2006) 423–431.
- [46] R.R. Meyer, A.I. Kirkland, R.E. Dunin-Borkowski, J.L. Hutchison, Experimental characterization of CCD cameras for HREM at 300 kV, Ultramicroscopy 85

- (2000) 9-13.
- [47] A.V. Martin, F.-R. Chen, W.-K. Hsieh, J.-J. Kai, S.D. Findlay, L.J. Allen, Spatial incoherence in phase retrieval based on focus variation, Ultramicroscopy 106 (2006) 914–924.
- [48] M.A. Schofield, M. Beleggia, Y. Zhu, G. Pozzi, Characterization of JEOL 2100F Lorentz-TEM for low-magnification electron holography and magnetic imaging, Ultramicroscopy 108 (2008) 625–634.
- [49] B. Freitag, M. Bischoff, H. Mueller, P. Hartel, H.S. von Harrach, Sub-nanometer resolution in field-free imaging using a Titan 80–300 with Lorentz lens and image Cs-corrector at 300 kV acceleration voltage, Microsc. Microanal. 15 (2) (2009) 184–185.
- [50] N.T. Nuhfer, A. Budruk, M. De. Graef, Aberration-corrected Lorentz microscopy, Microsc. Microanal. 16 (2) (2010) 142–143.
- [51] A.K. Petford-Long, M. DeGraef, Lorentz microscopy, in: E.N. Kaufmann (Ed.), Characterization of Materials, John Wiley and Sons, Inc., 2012, pp. 1–15 http://onlinelibrary.wiley.com/doi/10.1002/0471266965.com137/abstract.
- [52] E. Humphrey, C. Phatak, A.K. Petford-Long, M. De Graef, Separation of electrostatic and magnetic phase shifts using a modified transport-of-intensity equation, Ultramicroscopy 139 (2014) 5–12.
- [53] C. Phatak, A.K. Petford-Long, O. Heinonen, M. Tanase, M. De Graef, Nanoscale structure of the magnetic induction at monopole defects in artificial spin-ice lattices, Phys. Rev. B 83 (2011) 174431.
- [54] C. Phatak, Y. Liu, E. Begum Gulsoy, D. Schmidt, E. Franke-Schubert, A. K. Petford-Long, Visualization of the magnetic structure of sculpted threedimensional cobalt nanospirals, Nano Lett. 14 (2014) 759–764.